

NUMERICAL STUDY ON THE INFLUENCE OF TOP AND VALLEY SHAPE OF THE TRANSVERSE GROOVE ON THE DRAG REDUCTION RATE

ZHIPING LI, YUEREN ZUO

Research Institute of Aero-Engine, Beihang University, Beijing, China

HANAN LU

School of Energy and Power Engineering, Beihang University, Beijing, China

corresponding author Hanan Lu, e-mail: luhanan2013@163.com

LONG HE

Research Institute of Aero-Engine, Beihang University, Beijing, China

BO MENG

AECC Hunan Aviation Powerplant Research Institute, Zhuzhou, China

This study investigates the drag reduction effect and mechanism of modified transverse grooves by employing “Constant Width” and “Constant Height” filleting methods on the top and valley of two-dimensional transverse V -shaped grooves. Results revealed a significant increase in the total drag reduction rate, from 13.29% to 23.24%, when a constant width fillet was applied to the grooves top at $r_3 = 0.3/\sqrt{2}$ mm. However, minimal or negative effects were observed in other cases. These findings establish a preliminary theoretical basis for future transverse groove design and processing.

Keywords: grooves, drag reduction rate, flow control, optimized structure

1. Introduction

Amidst the exacerbation of energy scarcity, there is a growing emphasis on drag reduction strategies. Remarkably, a research conducted by NASA Langley Research Center highlighted that a mere 1% decrease in drag translates to a significant 5% to 10% augmentation in subsonic aircraft payload capacity (Bushnell, 1990). Delving into drag reduction performance, scholars have explored bio-inspired microstructures since the last century (Walsh and Lindemann, 1984). These microstructures are categorized into riblets and transverse grooves oriented parallel and perpendicular to the flow direction, respectively. Notably, current drag reduction investigations have predominantly focused on transverse grooves due to their impressive drag reduction attributes and versatile applicability (Sareen *et al.*, 2014; Ghazali *et al.*, 2016).

The drag reduction mechanism of transverse grooves has garnered scholarly attention. The MABS (Micro-Air Bearings) theory, initially developed by NASA (Bushnell, 1983) in the 1980s, posits that stable boundary vortices formed by a fluid within grooves act as bearings, akin to converting sliding friction into rolling friction, thereby reducing drag. Pan (1996) experimentally validated this theory and observed that these “bearings” attenuated vertical momentum exchange in the boundary layer without affecting the mainstream flow. Choi (1989) employed hotwire/film anemometry, flow visualization techniques and laser light sheets to investigate structural changes in the turbulent boundary layer near riblet surfaces. They noted a turbulence intensity reduction of up to 10%, which was further confirmed by DNS (direct numerical simulations) conducted by Choi *et al.* (1993). Subsequent research by other scholars (García-Mayoral and Jiménez, 2011a,b) entailed experimental and simulation studies to analyze flow

characteristics within the grooves and corroborated the vortex-related nature of drag reduction properties, aligning with the qualitative description of the MABS theory. These findings offer valuable insights into the drag reduction mechanisms associated with transverse grooves.

Other scholars focused on parametric studies of transverse grooves. Bai *et al.* (2016) conducted numerical simulations to investigate the drag reduction efficiency of four different geometries: V -shaped, zigzag, rectangular and semi-circular. They discovered that a V -shaped groove textured surface achieved the highest friction coefficient. Oak Ridge National Laboratory (Barbier *et al.*, 2012) conducted experimental tests on grooves of various sizes at low speeds and observed a drag reduction rate of 13% for a 1 mm deep groove. However, as the flow velocity increased, the secondary flow developed, leading to a lower drag reduction rate. Nevertheless, even for larger grooves, the drag reduction rate remained above 15%. To provide a quantitative theoretical foundation for groove parameter design, Li *et al.* (2022a) proposed a physical model that established the relationship between dimensionless depth of a transverse groove, dimensionless inflow velocity and drag reduction rate. They quasi-analytically solved for the optimal and maximum transverse groove depths based on Reynolds numbers. Moreover, the grooves exhibited favorable applications in heat transfer compared to flat plates (Belhocine and Wan Omar, 2015; Bilen *et al.*, 2009).

Parametric studies have promoted the engineering application of the grooves. However, little research has focused on the local structural optimization of such grooves. Recent experiments by Leidl *et al.* (2022) revealed that defects occurring in the microstructure, either due to processing or prolonged usage, could significantly affect drag reduction. We contend that the top and valley, also as the most subtle components within the grooves, possess the highest potential for machining errors and are susceptible to wear and contamination during usage. Hence, we aimed to investigate the influence of geometric modifications to the top and valley on the flow characteristics in the vicinity of the grooves. This study modified the shape of commonly used two-dimensional transverse V -grooves top and valley and analyzed the corresponding drag reduction effects through numerical simulations. The results shed light on the significance of these shape alterations in influencing the drag reduction rate. This research provides a theoretical basis for the future groove design and processing, enabling an improved performance in various applications.

2. Models and methods

2.1. Geometric modification of the transverse groove

From the study of Cui and Fu (2012), a symmetric V -shape is the simplest structure of transverse grooves and has certain improvement potential in the drag reduction effect. Consequently, a geometric prototype groove (V -shape) was selected, as shown in Fig. 1a, where the dimensions w and h denote width and height of the transverse groove. The flow state near the groove is visually represented by red lines.

The drag reduction model proposed by Li *et al.* (2022a) has high accuracy for Reynolds numbers below $2.18E5$. Consequently, a Reynolds number of $Re = 1.5E5$ is selected near the groove (incompressible). So, the dimensionless incoming flow velocity ($U_{\infty}^+ = U_{\infty}/u_{\tau}$) is 19.34, while the dimensionless height of the groove ($H^+ = Hu_{\tau}/\nu$) reaches approximately 10.26, resulting in the maximum drag reduction. Here, U_{∞} denotes the actual incoming flow velocity, H represents the groove depth, and u_{τ} is the friction velocity that characterizes turbulent shear stress and related parameters. In this case, the prototype groove depth is 0.5 mm. To maintain vortex stability within the groove, the prototype groove width W is set to 1 mm, ensuring an aspect ratio $AR = W/H$ of approximately 2 (Li *et al.*, 2022b).

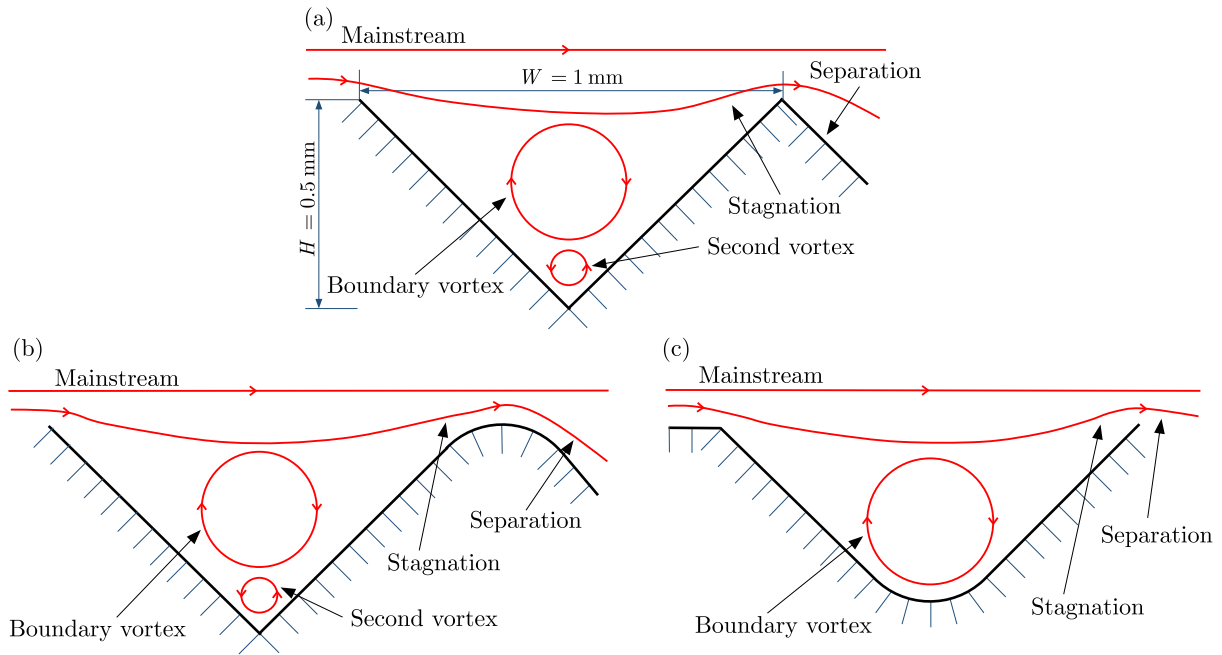


Fig. 1. Flow field with different geometry: (a) prototype groove, (b) fillet top, (c) fillet valley

In Fig. 1a, two vortices are exhibited in a single groove, differing in scale, position and direction. The small secondary vortex located at the groove valley experiences intense shearing against the wall, which is usually detrimental to the overall drag reduction effect. Meanwhile, a larger scale boundary vortex makes the boundary layer of the mainstream slip, acting akin to the “rolling bearing” (Bushnell, 1983). While, the mainstream stagnates at the windward side of the grooves and produces local separation at the leeward side, resulting in an extra pressure drag at the top.

From the above analysis, it can be concluded that the flow inside the grooves is influenced by geometry of the valley and top. Speculatively, modifying the fillet on the top and valley (Figs. 1b and 1c) could eliminate shear from the secondary vortex and weaken the high-pressure area caused by the boundary vortex. This modification has potential to significantly enhance the overall drag reduction rate of the grooves.

Considering the actual processing and other aspects, two kinds of fillet methods are finally adopted to optimize the top and valley geometry of the grooves:

- Constant Width (CW): Reduce the height of the individual groove and remain the width of geometry unchanged, as shown in Figs. 2a and 2c;
- Constant Height (CH): Expand the width of the individual groove and remain the height unchanged, as shown in Figs. 2b and 2d.

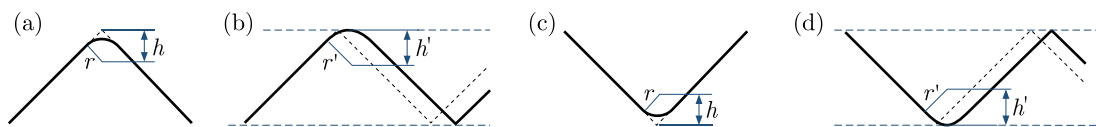


Fig. 2. Different fillet: (a) constant width top, (b) constant height top, (c) constant width valley, (d) constant height valley

In practical machining, these two geometric modification methods are easily attainable. For instance, in the case of metal groove machining, the desired modified geometry can be obtained by simply altering the shape of the cutting tool based on the prototype. This facilitates subsequent experimental validation and facilitates widespread application of the modified grooves on

a larger scale. Defects exceeding $60\%h$ (0.3 mm) in geometric changes are rare, thus not requiring further investigation.

The two methods involve maintaining the wall inclination constant, and h is the distance from the prototype groove vertex to the fillet center, whose relationship with the fillet radius as

$$h = \sqrt{2}r \quad h' = r' \quad (2.1)$$

The specific geometric modification scheme is outlined in Table 1, detailing the fillet location (FL), fillet radius (FR) and fillet method (FM).

Table 1. Geometric modification scheme

FL	FR [mm]	FM
Top	$r_1 = 0.05/\sqrt{2}$	CW
	$r_2 = 0.1/\sqrt{2}$	CW
	$r_3 = 0.3/\sqrt{2}$	CW
	$r'_1 = 0.05$	CH
	$r'_2 = 0.1$	CH
	$r'_3 = 0.3$	CH
Valley	$r_1 = 0.05/\sqrt{2}$	CW
	$r_2 = 0.1/\sqrt{2}$	CW
	$r_3 = 0.3/\sqrt{2}$	CW
	$r'_1 = 0.05$	CH
	$r'_2 = 0.1$	CH
	$r'_3 = 0.3$	CH

2.2. Computational domain and boundary conditions

A schematic representation of the computational domain and boundary conditions is presented in Fig. 3. The computational domain possesses a height and length of 500 mm, significantly larger than the boundary layer thickness. The freestream allows for the transition from a laminar to turbulent flow over the upstream smooth wall, which extends over a length of 365 mm. The downstream smooth wall with a length of 300 mm ensures minimal pressure perturbations at the outlet. Situated between the two smooth walls is a grooved wall, approximately 12 mm in length, comprising symmetric *V*-groove profiles. The grooves have an aspect ratio of 2 ($AR = W/H$) and a depth of 0.5 mm.

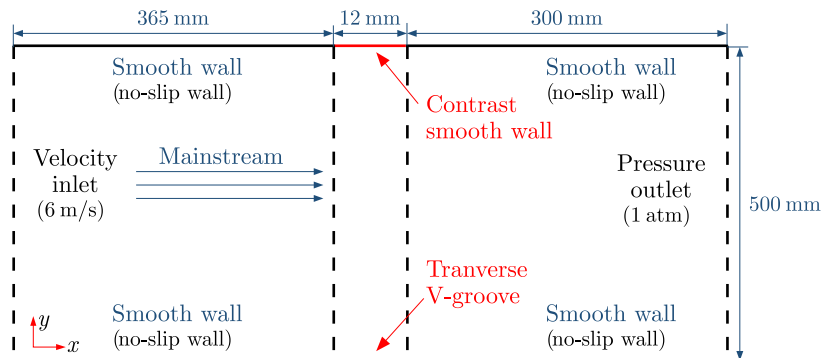


Fig. 3. Computational domain and boundary conditions

The computational fluid dynamics analysis (CFD) of the groove surface is performed using the Fluent 18.2 commercial software. The inlet boundary condition is defined as a constant

velocity of 6 m/s. And the upstream smooth wall extends for a length of 365 mm, resulting in minimal impact of pressure disturbances on the velocity inlet. The pressure outlet condition is set with a constant gauge pressure of 0 (Operating Pressure = 101325 Pa). Additionally, all smooth walls are assigned the no-slip wall condition. In simulation, the key lies in solving the Navier-Stokes equations as (Belhocine and Abdullah, 2019)

$$\frac{\partial}{\partial t}(\rho u_i) + \frac{\partial}{\partial x_j}(\rho u_i u_j) = -\frac{\partial p}{\partial x_i} + \frac{\partial \tau_{ij}}{\partial x_j} + \rho g_i + F_i \quad (2.2)$$

where p is the static pressure, τ_{ij} is the surface stress tensor, g_i and F_i are gravity and external volume force. To solve the system of partial differential equations composed of the Navier-Stokes equation, continuity equation and energy equation, numerical methods are required.

DeGroot *et al.* (2016) conducted an extensive investigation on a turbulent flow in grooved channels and their potential for reducing friction factors. They validated the RANS (Reynolds-Averaged Navier-Stokes) modeling approach by comparing it with DNS (direct numerical simulations), confirming its accuracy and computational efficiency for studying the turbulent flow in grooved channels. In this study, the steady Reynolds-Averaged Navier-Stokes approach is employed for CFD (computational fluid dynamics) simulations. The Reynolds-Averaged Navier-Stokes (RANS) method is extensively employed for tackling turbulent flow phenomena. It involves the temporal averaging of the governing Navier-Stokes equations to obtain a set of time-averaged equations. Subsequently, additional turbulence models are employed to account for the influence of turbulence on the flow. Considering that the Transition SST four-equation turbulence model is more sensitive to flow separation, pressure gradient, and can capture flow characteristics in the near-wall region well (Menter *et al.*, 2006; Aftab *et al.*, 2016), it is used to determine the flow field.

2.3. Grid delineation and independence study

The structured mesh shown in Fig. 4 is generated using the Ansys ICEM meshing tool. To ensure accurate boundary layer flow simulation, the Transition SST turbulence model requires the Y plus value below 1. In order to capture the flow details near the grooves $h = 0.5$ mm with enhanced precision, considering the Reynolds number and the physical parameters of the medium, the normal distance from the nodes of the first grid layer to the wall surface is set to 0.003 mm. Consequently, the actual Y plus range near the grooved wall falls within the range of 0.0599-0.06.

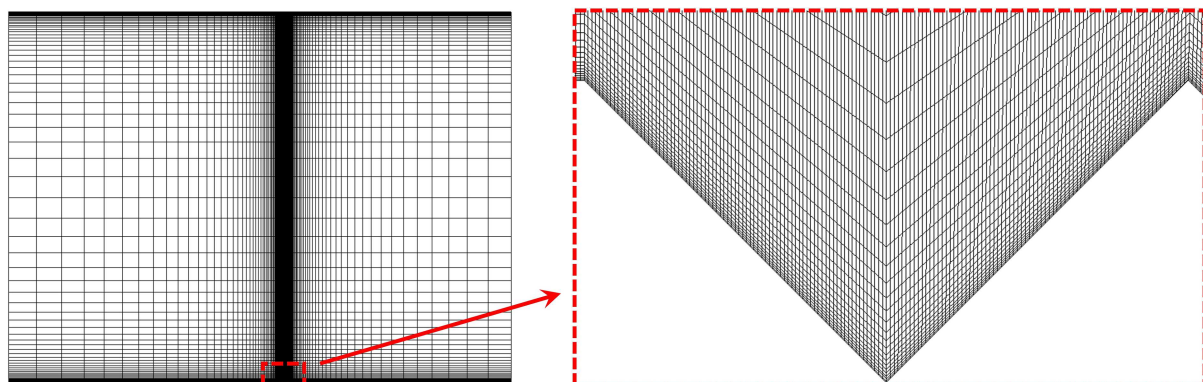


Fig. 4. Mesh distribution around the transverse V-groove

Figure 5 shows the relative error of the total drag of the grooved plate compared with that of the smooth plate at different grid-refinement levels. It can be observed that when the number of grid cells exceeds 297 463, the relative error for both drags remains below 0.05%.

Consequently, to strike a balance between the computational accuracy and resource efficiency, the subsequent calculations utilize approximately 297 463 grid cells to ensure accurate results while saving computational resources.

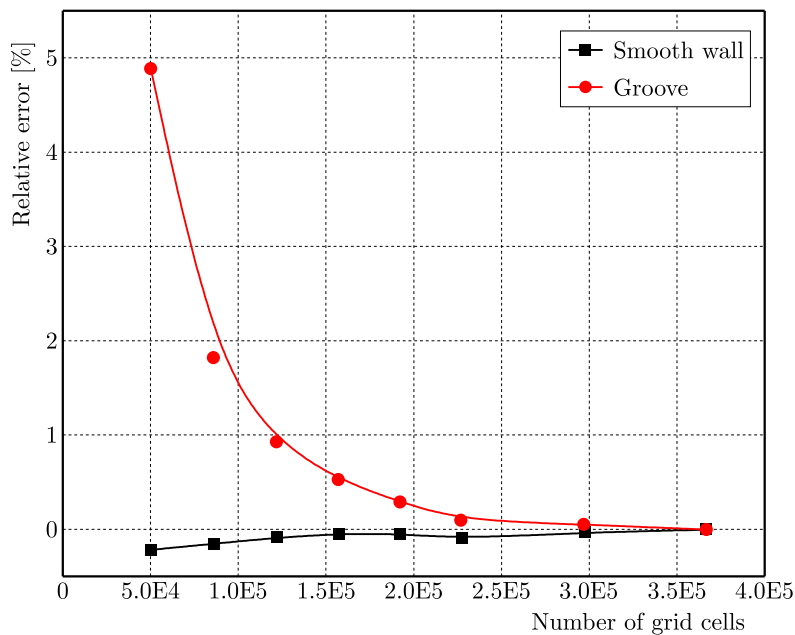


Fig. 5. Verification of grid independence

2.4. Numerical method validation

To assess the accuracy of the numerical method, a numerical simulation of a grooved plate with depth of 1.62 mm and width of 3.57 mm was conducted in a wind tunnel. The simulation results were then compared to relevant experimental data obtained by Ahmadi-Baloutaki *et al.* (2013), Fig. 6. When considering a turbulence intensity of 0.5% and a Reynolds number of 1.85E5, the relative errors between the numerical calculations and the experimental results were all below 5%. These findings, coupled with the conclusions drawn by DeGroot *et al.* (2016), validate the accuracy of the numerical method employed in this study for accurately predicting the drag reduction effect of transverse grooves.

3. Law of the drag reduction rate

The drag of a grooved plate is formed by viscous drag F_{CV} and pressure drag F_{CP} , defined as (Li *et al.*, 2022a)

$$F_{GV} = \int_0^{l_s} \boldsymbol{\tau} \cdot \mathbf{e}_x dl \quad F_{CP} = \int_0^{l_s} (p - p_\infty) \mathbf{n} \cdot \mathbf{e}_x dl \quad (3.1)$$

Here, $\boldsymbol{\tau}$ is the shear stress on the wall surface, \mathbf{e}_x is the unit vector along the x direction (flow direction), l_s is length of the wetted wall of grooves, p_∞ is the ambient pressure, l is the unit area along the groove wall, and \mathbf{n} represents the normal vector to the wall. Further, the drag reduction rate can be denoted by Eq. (3.2) (Li *et al.*, 2022a), where F_G and F_R represent the drag of the grooved and smooth plate, respectively

$$\eta = \frac{F_G - F_R}{F_R} = \frac{F_{GV} - F_R}{F_R} + \frac{F_{GP}}{F_R} = \eta_v + \eta_p \quad (3.2)$$

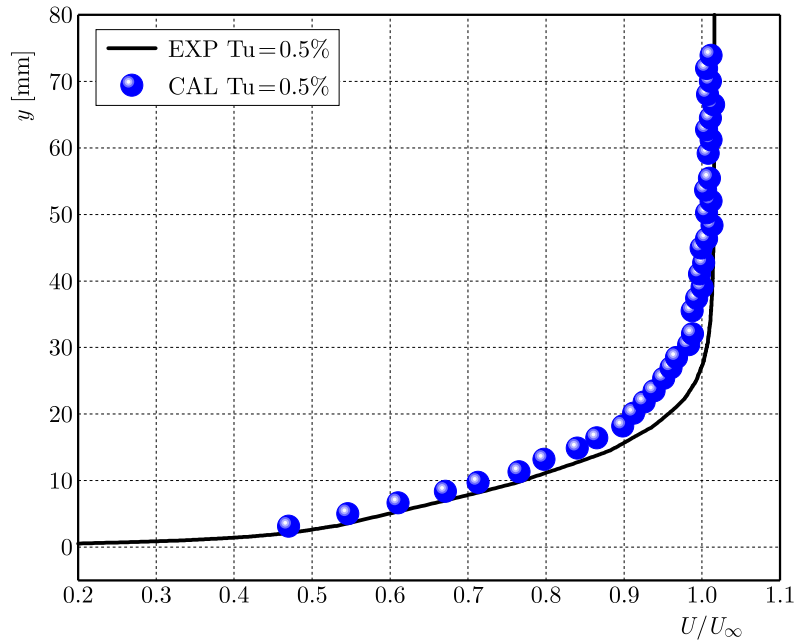


Fig. 6. The comparison of numerical and experimental results (Ahmadi-Baloutaki *et al.*, 2013)

Here, η_v denotes the reduction rate of viscous drag which is negative. η_p denotes the increased rate of pressure drag which is positive. A negative value of η indicates a reduction in the total drag with a higher absolute value indicating a higher drag reduction rate. The drag reduction characteristics of the grooves with different fillet radii (FR) after using two fillet methods (FM), constant height (CH) and constant width (CW), at two fillet positions (FP), top and valley, are presented in Table 2.

Table 2. Calculation results of drag reduction characteristics

FP	FR	FM	η_p	η_v	η
Prototype	$r_0 = 0$	-	78.24%	-91.53%	-13.29%
Top	r_1	CW	65.38%	-80.62%	-15.24%
	r_2	CW	59.22%	-76.16%	-16.94%
	r_3	CW	44.45%	-67.69%	-23.24%
	r'_1	CH	64.95%	-77.26%	-12.31%
	r'_2	CH	59.38%	-70.90%	-11.52%
	r'_3	CH	46.28%	-56.03%	-9.77%
Valley	r_1	CW	78.14%	-91.49%	-13.35%
	r_2	CW	78.23%	-91.55%	-13.32%
	r_3	CW	81.60%	-93.21%	-11.62%
	r'_1	CH	78.80%	-92.06%	-13.26%
	r'_2	CH	79.32%	-92.71%	-13.39%
	r'_3	CH	82.14%	-95.74%	-13.60%

3.1. Fillet top

The calculation results shown in Table 2 indicate that the geometric modifications at the top of the groove significantly impact the drag reduction rate, consistent with findings reported for riblets in the previous studies (Leitl *et al.*, 2022). Comparing the cases with a constant height, the grooves exhibit improved drag reduction effects when filleted using a constant width.

Among the existent constant width cases, the drag reduction rate increases with the increasing fillet radius, with a substantial increase from 13.29% to 23.24% observed when the fillet radius reaches r_3 . Conversely, when filleted using a constant height, the grooves display a lower drag reduction rate compared to the prototype grooves, primarily due to the greater decline in the absolute value of η_v .

In terms of specific changes in the drag reduction rate, the fillet top results in a decrease of η_p (cost) and the absolute value of η_v (benefit). Ultimately, the actual variation in the drag reduction rate is determined by the delicate balance between the benefits and costs associated with these changes.

3.2. Fillet valley

The influence of filleting the valley on the drag reduction rate of the groove is relatively minimal compared to the filleting of the top. From the perspective of η_v , η_p and η , when the fillet radius is small, the variation of these values with the two fillet methods are almost the same compared with the prototype groove. While the fillet radius reaches r_3 , the η_p of the groove in the constant width cases suddenly significantly increases and the absolute value of η_v increases less, leading to a reduction in the drag reduction rate from 13.29% to 11.62%.

While this Section presents the observed patterns of the drag reduction ratio in fillet transverse grooves based on the changes in η_v and η_p , it does not provide an explanation for these variations. In the upcoming Section, we delve into the flow details to uncover the underlying mechanisms that drive these changes.

4. Mechanism analysis

4.1. Characteristics of drag reduction induced by the fillet top

4.1.1. Fillet top and pressure drag

Figure 7 describes the pressure distribution in a unit groove on the wall with different fillet radii at the top. In the vicinity of the prototype groove (Fig. 7a), a region of high pressure is observed on the windward side of the top, while a localized low-pressure region is present on the leeward side. In Figs. 7h and 7i, these regions manifest as sharp positive and negative pressure peaks, respectively, at the top of the prototype groove r_0 . Filleting the top with a constant width leads to a more uniform pressure distribution on both sides of the transverse groove, as depicted in Figs. 7b, 7d, 7f, and 7h. The drag reduction effect improves with the increasing fillet radius. For instance, in Fig. 7h, with a fillet radius of r_3 , the difference between the positive and negative peaks of gauge pressure is approximately 0.05 Pa, whereas on the prototype groove, this difference reaches 0.45 Pa. The closer pressure on either side near the top of the groove signifies a lower pressure drag in that region.

Filleting the top of the groove with a constant height also leads to a reduction in pressure peaks, as shown in Fig. 7i, although not as much as in the constant width method. In the constant height cases, the minimum value of differences between the positive and negative peaks is 0.12 (at r'_3), which is nearly twice the corresponding value achieved by the constant width filleting. However, the constant height method widens the individual grooves, resulting in wider regions of the local low and high pressure. This leads to a decrease in pressure gradient. Consequently, the actual reduction in pressure drag achieved by this fillet method is comparable to that of the constant width method.

The streamline patterns depicted in Fig. 8 provide further insights into the underlying mechanism behind the changes in the drag reduction rate after filleting. It is evident that the streamlines exhibit periodic variations in the response to the groove structure. In Fig. 8a, as the fluid

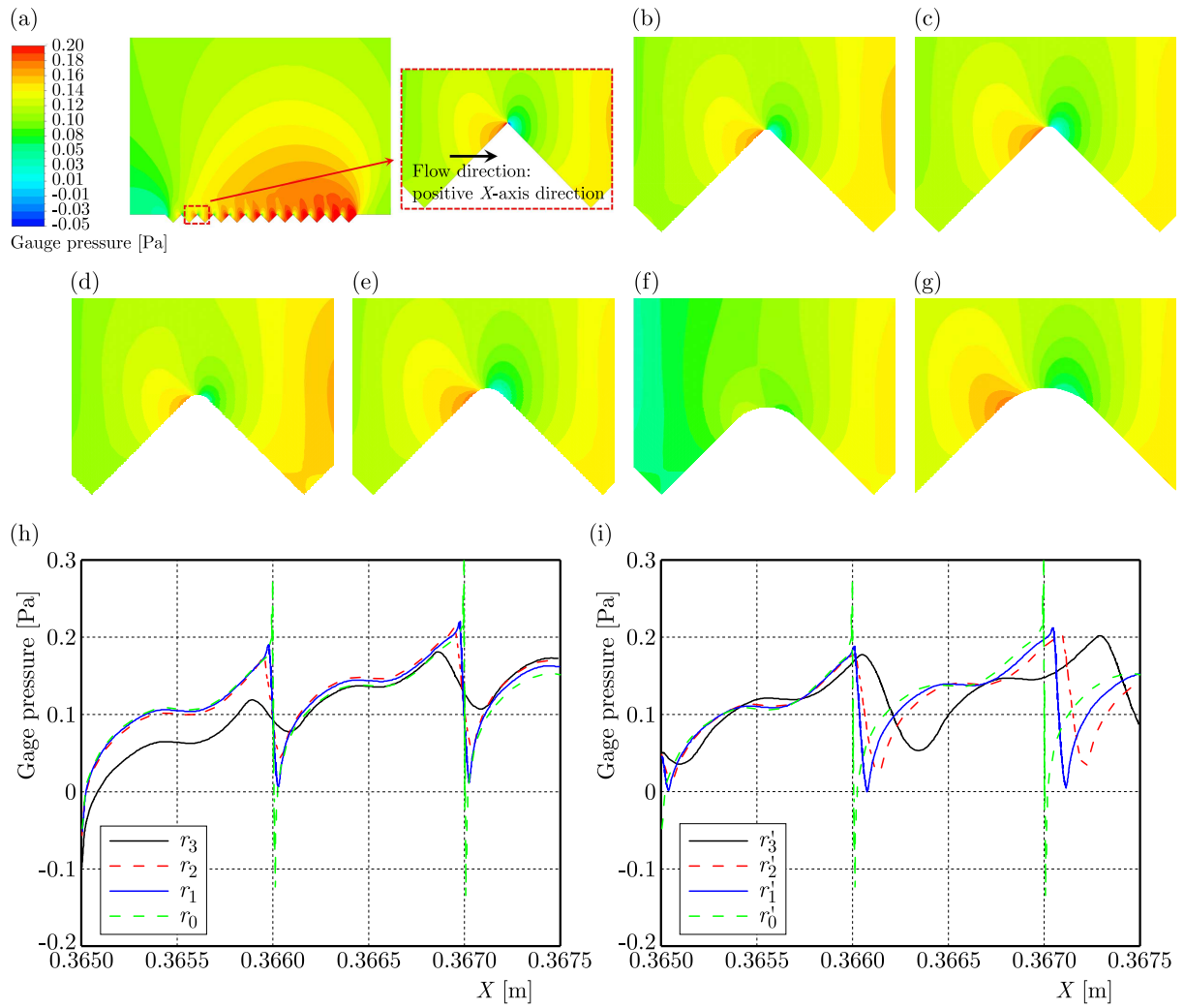


Fig. 7. Pressure distribution with the fillet top: (a) prototype groove r_0 , (b) CW r_1 , (c) CH r_1' , (d) CW r_2 , (e) CH r_2' , (f) CW r_3 , (g) CH r_3' , (h) CW, (i) CH

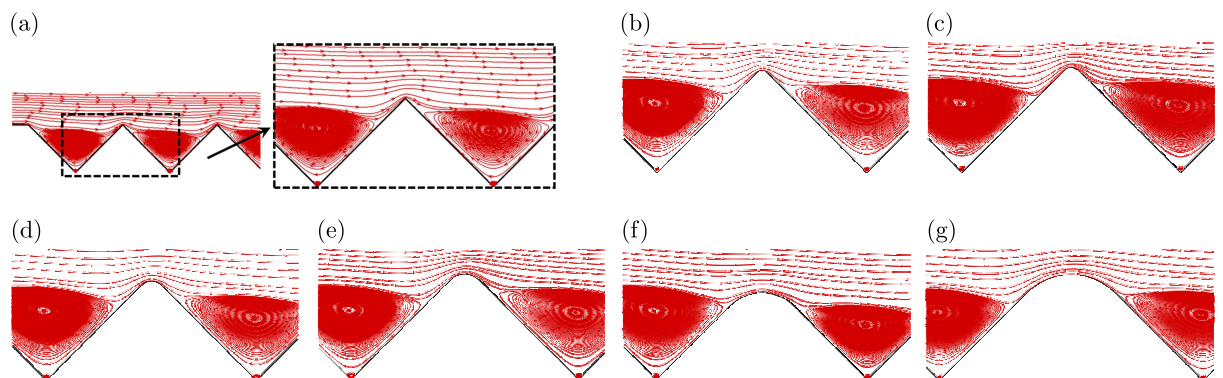


Fig. 8. Streamlines with the fillet top: (a) prototype groove r_0 , (b) CW r_1 , (c) CH r_1' , (d) CW r_2 , (e) CH r_2' , (f) CW r_3 , (g) CH r_3'

enters the V-shaped groove and forms a vortex, it experiences stagnation on the windward side of the groove top, leading to generation of a high-pressure region. As the fluid crosses the top, a sharp turning angle induces separation, resulting in a local low-pressure region. However, when the groove is filleted either by a constant height or constant width, the turning structure becomes

smoother, mitigating the stagnation and separation effects. Therefore, the pressure distribution on both sides of the groove top becomes more uniform, and the streamlines are closer to the geometric structure, resulting in a reduced pressure drag at the top of the groove.

4.1.2. Fillet top and viscous drag

Based on the above analysis, it is evident that the pressure drag of the V -groove decreases with both the constant height and constant width filleting methods. However, the drag reduction rate of the top filleted by the constant height is inferior to that of the prototype groove, as shown in Table 2. Hence, further investigation is required to understand the correlation between the reduction in the drag reduction rate and wall shear stress.

Figure 9 presents the wall shear stress distribution on the filleted top of the groove. It is evident that the wall shear stress follows a periodic pattern corresponding to the groove structure. The shear stress near the valley exhibits M shaped peaks, which are higher than the corresponding smooth wall shear stress. The fillet top has a little impact on the positive shear stress region near the M peaks, particularly in the constant width cases. The shear stress at the top is represented by a sharp negative peak. With an increase in the fillet radius, the peak shear stress near the groove top significantly decreases, resulting in a reduction in the extent of negative shear stress and an increase in the total viscous drag. In the constant height cases, the range of wall shear stress exceeding that of the smooth wall also increases, leading to a sharp rise in the total drag. This observation indicates that while filleting by the constant height reduces the pressure drag of the groove, it substantially increases the viscous drag, resulting in an inferior drag reduction rate compared to the prototype groove.

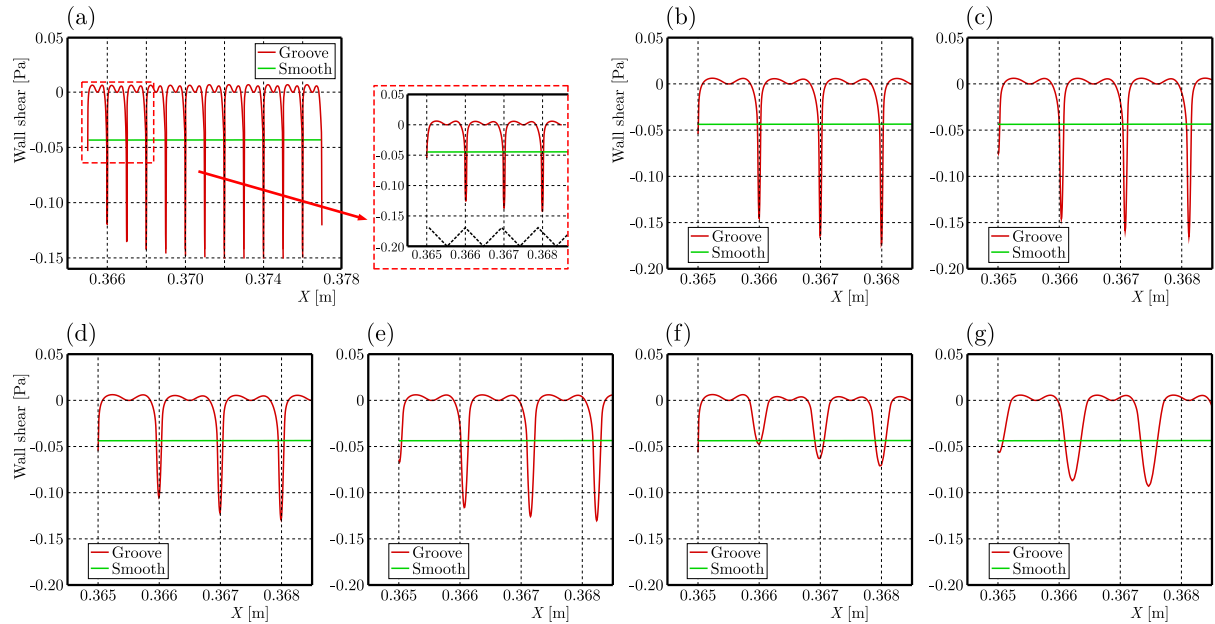


Fig. 9. Wall shear distribution with the fillet top: (a) prototype groove r_0 , (b) CW r_1 , (c) CH r'_1 , (d) CW r_2 , (e) CH r'_2 , (f) CW r_3 , (g) CH r'_3

4.2. Characteristics of drag reduction induced by the fillet valley

4.2.1. Fillet valley and pressure drag

The pressure distribution in Fig. 10 reveals that the fillet valley has almost no major effect on the pressure distribution near the V -groove when the fillet radius is small, resulting in slight changes to the local pressure. In the constant width cases, the pressure distribution curves of

the fillet groove almost coincide with that of prototype groove (Fig. 10h). For instance, when the fillet radius reaches r_2 , the overall pressure variation compared to the prototype groove is within 0.02 Pa. Similarly, in the constant height cases, the pressure peaks hardly change after filleting at r'_1 and r'_2 . However, as the fillet radius increases, the effect of local pressure becomes more pronounced. For example, in the constant width cases, when the fillet radius reaches r_3 , and in the constant height cases, when it reaches r'_3 , the positive and negative pressure peaks in Figs. 10h and 10i, respectively, are significantly larger than those in the prototype grooves. In these cases, the pressure drag is higher.

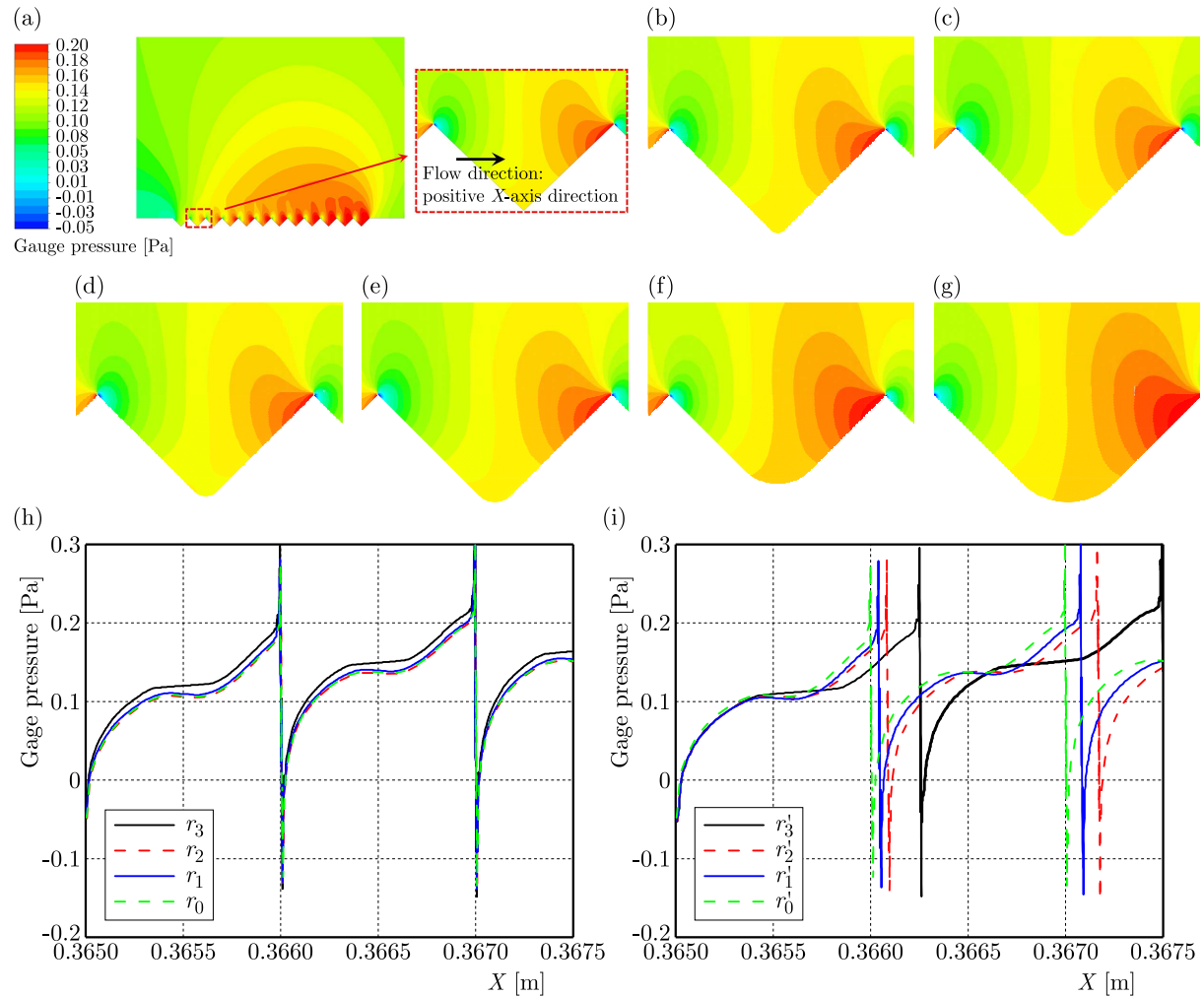


Fig. 10. Pressure distribution with the fillet valley: (a) prototype groove r_0 , (b) CW r_1 , (c) CH r'_1 , (d) CW r_2 , (e) CH r'_2 , (f) CW r_3 , (g) CH r'_3 , (h) CW, (i) CH

The streamline diagram in Fig. 11 illustrates that filleting the groove leads to a closer fit of the streamline with the corner of the turn, resulting in the elimination of secondary vortex structures and a moderation of velocity as well as pressure gradient at the groove valley. The fluid near the valley is influenced by the central vortex and moves in the clockwise direction. While the reduction in pressure gradient suggests a potential decrease in the pressure drag, it is important to note, as stated in the earlier findings in Section 4.2, that this advantage is very small and may even have a negative impact when the fillet radius is large. Moreover, the reduction in the velocity gradient may affect the viscous drag, which will be further discussed in the subsequent Section.

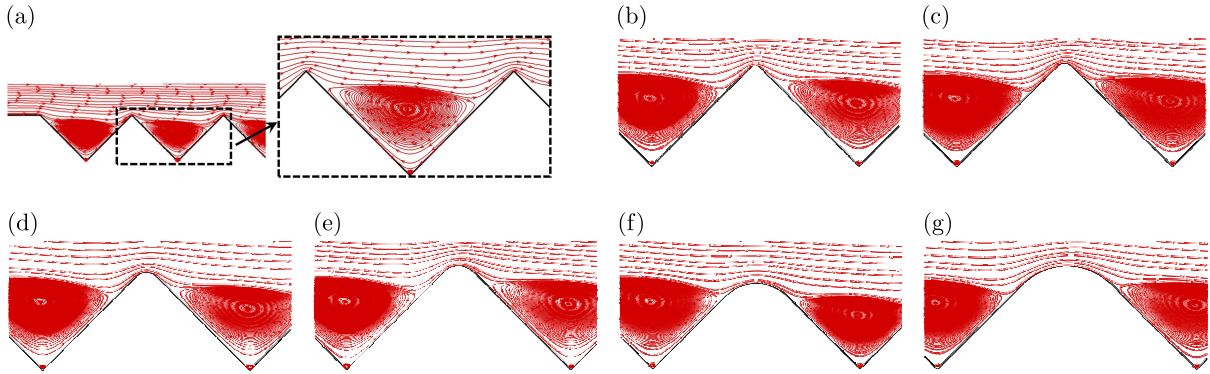


Fig. 11. Streamline distribution with the fillet valley (a) prototype groove r_0 , (b) CW r_1 , (c) CH r_1' , (d) CW r_2 , (e) CH r_2' , (f) CW r_3 , (g) CH r_3'

4.2.2. Fillet valley and viscous drag

Figures 12a-12e demonstrate that the wall shear stress in cases with small fillet radius remains largely unchanged compared to the prototype groove, corroborating the findings in Table 2. Combined with the streamline diagram shown in Fig. 11, the absence of secondary vortex structures leads to an increase of the valley range of the M peak, indicating a reduction in the viscous drag. This reduction becomes particularly prominent with a larger fillet radius, as depicted in Figs. 12f and 12g. Consequently, in the cases with a large fillet radius, while the elimination of secondary vortex structures may contribute to an increase in the pressure drag at the groove valley, the decrease in the viscous drag can offset this effect, ultimately resulting in a higher drag reduction rate.

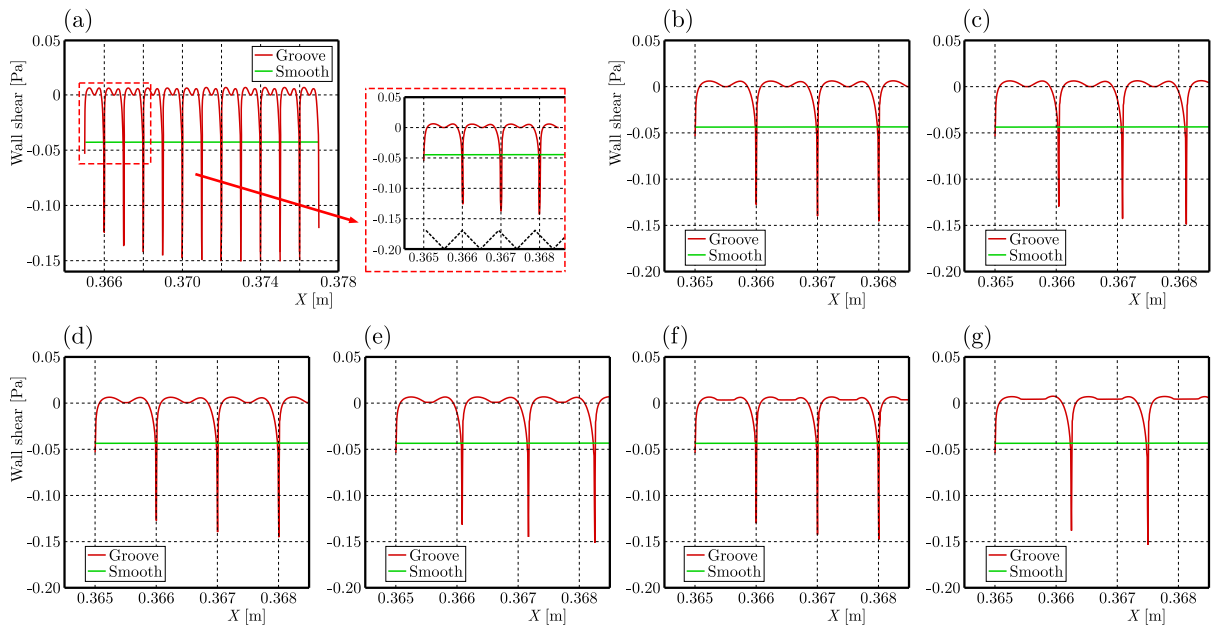


Fig. 12. Wall shear distribution with the fillet valley: (a) prototype groove r_0 , (b) CW r_1 , (c) CH r_1' , (d) CW r_2 , (e) CH r_2' , (f) CW r_3 , (g) CH r_3'

5. Conclusion

In this study, numerical simulations were performed to investigate flow characteristics of a flat plate with two-dimensional V-shaped transverse grooves. The effects of two filleting methods, namely “Constant Width” (CW) and “Constant Height” (CH), at the top and valley of the

grooves were examined to understand the changes in the flow mechanism. The key findings are summarized as follows:

- The filleting of the top of transverse grooves has an obvious impact on the drag reduction characteristics compared to the prototype grooves plate. Filleting the top leads to a decrease in the rate of increase in the pressure drag η_p , but it also reduces the absolute value of the viscous drag reduction rate η_v . When applying a constant width filleting, the total drag reduction rate significantly increases with a larger fillet radius, reaching a maximum of 23.24% at $r_3 = 0.3/\sqrt{2}$ mm from 13.29% due to a faster decrease in the cost (pressure drag). Conversely, filleting the top using a constant height results in a larger rise in the viscous drag, leading to a decrease in the total drag reduction rate with the increasing fillet radius.
- Both constant width and constant height filleting methods eliminate the secondary steady vortex at the valley of the groove, thereby reducing the viscous drag. However, at a larger fillet radius, these methods also increase the rate of increase in the pressure drag, leading to a reduction in the overall drag reduction rate. In the case of the constant height filleting, the drag reduction rate remains relatively unchanged compared to the prototype grooved plate, as the benefits and costs are balanced. On the other hand, the constant width filleting results in a lower total drag reduction rate of 11.62% at $r_3 = 0.3/\sqrt{2}$ mm due to the higher η_p .

In summary, our study analyzed the impact of modifying the top and groove of transverse grooves on drag reduction performance. We found that geometric changes of the top, resembling the “constant width” approach discussed earlier, are effective in improving the actual drag reduction performance of the grooves. So, engineers can intentionally design grooves with similar geometries to enhance the drag reduction performance even further. In the future, we will focus on investigating the impact of other forms of geometric variations on the drag reduction performance after a long-term use of the grooves.

Acknowledgements

This work was supported by the National Natural Science Foundation of China (No. 52176032), National Science and Technology Major Project (2017-k-0005-0016).

References

1. AFTAB S.M.A., MOHD RAFIE A.S., RAZAK N.A., AHMAD K.A., 2016, Turbulence model selection for low Reynolds number flows, *PLOS One*, **11**, 4, e0153755
2. AHMADI-BALOUTAKI M., CARRIVEAU R., TING D.K., 2013, Effect of free-stream turbulence on flow characteristics over a transversely-grooved surface, *Experimental Thermal and Fluid Science*, **51**, 56-70
3. BAI Q., BAI J., MENG X., JI C., LIANG Y., 2016, Drag reduction characteristics and flow field analysis of textured surface, *Friction*, **4**, 165-175
4. BARBIER C., JENNER E., D'URSO B., 2012, Drag reduction with superhydrophobic riblets, *ASME International Mechanical Engineering Congress and Exposition*, **45240**, 199-205
5. BELHOCINE A., ABDULLAH O.I., 2019, Numerical simulation of thermally developing turbulent flow through a cylindrical tube, *The International Journal of Advanced Manufacturing Technology*, **102**, 2001-2012
6. BELHOCINE A., WAN OMAR W., 2015, Numerical study of heat convective mass transfer in a fully developed laminar flow with constant wall temperature, *Case Studies in Thermal Engineering*, **6**, 116-127

7. BILEN K., CETIN M., GUL H., BALTA T., 2009, The investigation of groove geometry effect on heat transfer for internally grooved tubes, *Applied Thermal Engineering*, **29**, 4, 753-761
8. BUSHNELL D., 1983, Turbulent drag reduction for external flows, *21st Aerospace Sciences Meeting*, p. 227
9. BUSHNELL D., 1990, Supersonic aircraft drag reduction, *21st Fluid Dynamics, Plasma Dynamics and Lasers Conference*, p. 1596
10. CHOI H., MOIN P., KIM J., 1993, Direct numerical simulation of turbulent flow over riblets, *Journal of Fluid Mechanics*, **255**, 503-539
11. CHOI K.S., 1989, Near-wall structure of a turbulent boundary layer with riblets, *Journal of Fluid Mechanics*, **208**, 417-458
12. CUI J., FU Y., 2012, A numerical study on pressure drop in microchannel flow with different bionic micro-grooved surfaces, *Journal of Bionic Engineering*, **9**, 1, 99-109
13. DEGROOT C.T., WANG C., FLORYAN J.M., 2016, Drag reduction due to streamwise grooves in turbulent channel flow, *Journal of Fluids Engineering*, **138**, 12
14. GARCÍA-MAYORAL R., JIMÉNEZ J., 2011a, Drag reduction by riblets, *Philosophical Transactions of the Royal Society A: Mathematical, Physical and Engineering Sciences*, **369**, 1940, 1412-1427
15. GARCÍA-MAYORAL R., JIMÉNEZ J., 2011b, Hydrodynamic stability and breakdown of the viscous regime over riblets, *Journal of Fluid Mechanics*, **678**, 317-347
16. GHAZALI M.I., HARUN Z., GHOPA W.W., ABBAS A.A., 2016, Computational fluid dynamic simulation on NACA 0026 airfoil with V-groove riblets, *International Journal on Advanced Science, Engineering and Information Technology*, **6**, 4, 529-533
17. JIANG L., YANG W., XIE L., LIU Y., WANG X., WU X., ZHOU F., HU H., 2023, Experimental study on mechanism of stable drag reduction with hydrogel interface, *Tribology International*, **178**, 108013
18. LEITL P.A., SHIRAISHI M., FLANSCHGER A., TSUCHIHASHI S., MARN A., SCHRECK S., ICHINOSE G., SHIBAZAKI Y., BENAUER R., PRAMSTRAHLER S., 2022, Numerical and experimental investigation of lasered riblets on turbine exit guide vanes and the impact on the performance, *AIAA Scitech 2022 Forum*, p. 917
19. LI Z., HE L., ZHENG Y., 2022a, Quasi-analytical solution of optimum and maximum depth of transverse V-groove for drag reduction at different Reynolds numbers, *Symmetry*, **14**, 2, 342
20. LI Z., HE L., ZUO Y., MENG B., 2022b, Analytic solution of optimal aspect ratio of bionic transverse V-groove for drag reduction based on vorticity kinetics, *Aerospace*, **9**, 12, 749
21. MENTER F.R., LANGTRY R.B., LIKKI S.R., SUZEN Y.B., HUANG P.G., VÖLKER S., 2006, A correlation-based transition model using local variables – Part I: model formulation, *Journal of Turbomachinery*, **128**, 3, 413-422
22. PAN J., 1996, An experimental approach to drag reduction of transverse ribbons on turbulent flow, *Acta Aerodynamica Sinica*, **14**, 3, 304-310
23. PASHA A.A., ABDUL RAHEEM M., ISLAM N., JUHANY K.A., MUSHTAQ A., HALKARNI S.S., 2019, CFD study of variable property effects on laminar micro-convective heat transfer, *Arabian Journal for Science and Engineering*, **44**, 5961-5972
24. SAREEN A., DETERS R.W., HENRY S.P., SELIG M.S., 2014, Drag reduction using riblet film applied to airfoils for wind turbines, *Journal of Solar Energy Engineering*, **136**, 2
25. WALSH M., LINDEMANN A., 1984, Optimization and application of riblets for turbulent drag reduction, *22nd Aerospace Sciences Meeting*, p. 347